Laterally vibrating resonator based elasto-optic modulation in aluminum nitride

Siddhartha Ghosh[a] and Gianluca Piazza
Department of Electrical and Computer Engineering, Carnegie Mellon University, Pittsburgh, Pennsylvania 15213, USA

(Received 1 February 2016; accepted 21 March 2016; published online 6 June 2016)

An integrated strain-based optical modulator driven by a piezoelectric laterally vibrating resonator is demonstrated. The composite structure consists of an acoustic Lamb wave resonator, in which a photonic racetrack resonator is internally embedded to enable overlap of the guided optical mode with the induced strain field. Both types of resonators are defined in an aluminum nitride (AlN) thin film, which rests upon a layer of silicon dioxide in order to simultaneously define optical waveguides, and the structure is released from a silicon substrate. Lateral vibrations produced by the acoustic resonator are transferred through a partially etched layer of AlN, producing a change in the effective index of the guided wave through the interaction of the strain components with the AlN elasto-optic (p) coefficients. Optical modulation through the elasto-optic effect is demonstrated at electromechanically actuated frequencies of 173 MHz and 843 MHz. This device geometry further enables the development of MEMS-based optical modulators in addition to studying elasto-optic interactions in suspended piezoelectric thin films.
[http://dx.doi.org/10.1063/1.4945356]

The interaction of acoustic waves with light provides a useful resource to perform optical signal processing in a variety of applications. Acoustic waves are well-suited for operation in radio frequencies (RF), and diffraction effects produced by acousto-optic interaction have resulted in the demonstration of various optical devices including modulators, filters, and spectrum analyzers.[1,2] In recent years, several types of acousto-optic interactions have been demonstrated in a wide variety of devices, including the use of optomechanical forces[3] and stimulated Brillouin scattering.[4] Among crystalline materials exhibiting optical activity, however, a great deal of interest has focused on non-centrosymmetric films for the ability to piezoelectrically transduce acoustic waves.[5] This has led to demonstrations of devices that operate by physically deforming an optical cavity in the presence of an acoustic wave.[6–8] While displacements decrease with increasing frequencies of operation, mechanical strain remains relatively constant and can serve as a potentially significant contributor to a modulatory device. The elasto-optic (photoelastic) effect has thus been considered in optomechanical resonators[9,10] and forms the basis of several devices that have been demonstrated with the use of surface acoustic wave (SAW) transducers.[11–13] However, drawbacks to using SAWs (Rayleigh waves) include low electromechanical coupling efficiency, and limited spatial overlap of the acoustic mode with a guided optical mode. While electromechanical coupling with SAWs is typically improved with choice of piezoelectric substrate, these devices are not always possible to integrate with CMOS electronics. In addition, Rayleigh waves propagate on the surface of the interaction medium,[14] while the optical wave is typically centered in the thickness of the thin film structure. On the other hand, the use of a Lamb wave, such as those utilized in laterally vibrating contour mode resonators,[15,16] enables uniform strain distribution in the plane of the thin film. By

[a]Electronic mail: sidghosh@cmu.edu

overlapping an optical mode with strains generated in this type of resonant acoustic device, it is possible to produce a new type of modulator which can also easily scale to higher frequencies of operation through the lithographic definition of in-plane electrodes.

In order to demonstrate this concept, we pattern devices in thin films of aluminum nitride (AlN). On account of its wurtzite crystal structure, AlN has been a popular material for piezoelectric devices[15] and simultaneously exhibits relatively high elasto-optic coefficients.[17] Furthermore, it has been used to demonstrate optically resonant structures with integrated waveguides,[18] as well as electro-optic modulation.[19] The combination of these features allows us to produce a device in which the various refractive index modulation effects coincide in a rib waveguide that is co-located in an acoustic resonator. Sensitivity to changes in the refractive index is increased by simultaneously confining the traveling optical wave in a photonic resonator, which facilitates experimental measurements. A photonic resonator geometry that is compatible with the commonly used rectangular plate of the laterally vibrating acoustic resonator is a racetrack resonator. Similar to what has been shown for racetrack resonators configured for electro-optic modulation,[20] here we set one of the racetrack arms to be the integrated rib waveguide where the acoustic mode may overlap. Using this approach, we can concurrently operate the two types of resonators (acoustic and photonic) and observe optical modulation on account of refractive index changes induced in the rib waveguide structure that is common to both. In this work, we demonstrate an integrated two-port device, in which RF excitation is supplied to the first port, and a modulated optical signal is measured at the output of the photonic resonator.

Scanning electron microscope (SEM) images of the fabricated devices are shown in Fig. 1, along with the adjoining test setup used to probe the devices. Following the design of a laterally vibrating piezoelectric contour mode resonator (CMR),[15,16] the AlN film is sandwiched between top and bottom electrodes, and excited to vibrate in a width extensional mode through the d_{31} piezoelectric coefficient. The device operational frequency is set by the lateral dimensions (specifically the electrode pitch), which determines the acoustic wavelength of the vibrational mode. To exploit this geometry for strain-based modulation, we modify the resonator basic structure. In a conventional CMR, electrodes are alternately connected to ground and signal, generating lateral expansion and compression in adjacent fingers of the device. This produces maximal lateral displacements at the ends of the AlN plate. The corresponding mechanical strain (90° out of phase with the displacement) is thus maximized directly below the electrodes. As a result, optimal placement for a guided optical mode would correspond to the position of an electrode. For the optical waveguide integrated in the CMR to form part of a photonic resonator, the original CMR plate width is extended by half an acoustic wavelength on both ends. This allows the waveguide to be positioned where the next electrode would be naturally centered in a plate that is one acoustic wavelength wider. The waveguide integrated in the CMR body simultaneously forms part of a photonic resonator by closing the loop (as in a racetrack) outside the bounds of the vibrating structure. This allows a guided optical mode to remain isolated, while partially interacting with the excited Lamb wave. To maintain symmetry in the device, a waveguide is defined on both ends of the vibrating plate, but only one is "active" (part of a racetrack resonator). A schematic of the device cross-section, illustrating the extension of the conventional CMR and integrated waveguide placement is shown in Fig. 2.

Using this geometry for the device structure, the modulation produced through the change in refractive index of the integrated waveguide can be determined. In a piezoelectric material, the index ellipsoid may be modified through the elasto-optic and electro-optic effects. The refractive index change due to the presence of strain (S) and electric (E) fields is given by

$$\Delta\left(\frac{1}{n^2}\right)_i = p_{ij}S_j + r_{ik}E_k \qquad i,j = 1,2,\ldots,6, k = 1,2,3, \tag{1}$$

where p_{ij} and r_{ik} are the elasto-optic and electro-optic tensors, respectively. In the integrated waveguide, we consider a propagating optical mode with transverse electric (TE) polarization. This is based on the design of grating couplers and the integrated rib waveguide that are used to couple into the photonic resonator cavity.[8] Since the electric field of the TE mode is in the x ("1") direction, the relevant refractive index change is Δn_1. The AlN used in the device belongs to the *6mm* hexagonal point group, for which several elements of the tensors are zero due to symmetry. Likewise, only the

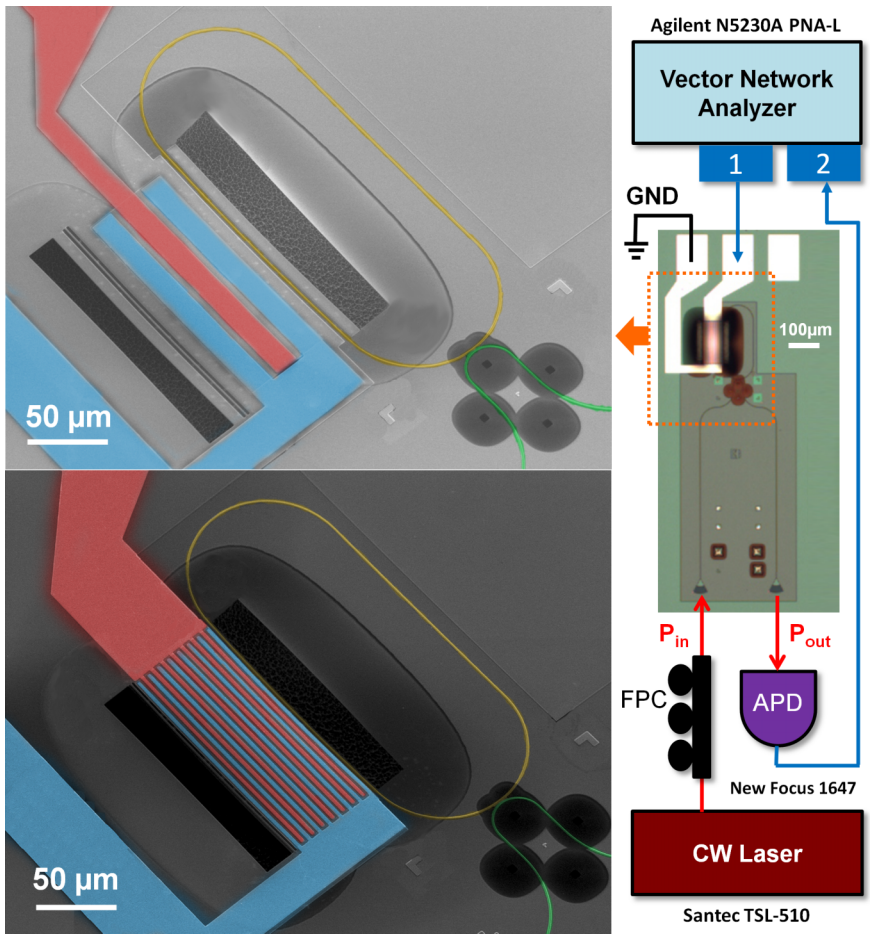

FIG. 1. (Left) SEM images of fabricated AlN elasto-optic modulation device with acoustic wavelength of 20 μm (top) and 8 μm (bottom). Colored features include ground (blue) and signal (red) electrodes, photonic racetrack resonator with embedded waveguide section (yellow) and bus rib waveguide (green). (Right) Experimental setup used to measure elasto-optic modulation with ground-signal-ground pads and grating couplers for RF and optical probing, respectively.

field components directed in the plane of the device's cross-section contribute to the change in n_1. Taking this into account, it is possible to derive a simplified expression for the change in refractive index experienced by the propagating acoustic wave as

$$\Delta n_1 = -\frac{1}{2} {n_1}^3 \left(p_{11} S_1 + p_{13} S_3 + r_{13} E_3\right), \tag{2}$$

where $p_{11} = -0.1$, $p_{13} = -0.019$, and $r_{13} = 0.67$ pm/V for AlN.[17,21] In order to estimate the effective contributions of the strain and electric fields, a finite element method simulation was conducted to determine a weighted average against the guided optical mode. For strain S_j, the effective strain contributing to the modulation can be described by $S_{j,eff} = \frac{\iint S_j E_{x,op}^2 dxdz}{\iint E_{x,op}^2 dxdz}$, where $E_{x,op}$ describes the optical field distribution for the TE polarized wave. A similar expression may be considered for $E_{3,eff}$, so as to include the effect of the electro-optic coefficient.

FEM simulations using COMSOL are shown for the mechanical mode at 843 MHz (acoustic wavelength = 8 μm) and the TE optical mode in the racetrack waveguide in Fig. 2. The laterally vibrating wave is simulated with a 2D frequency domain analysis of the device cross-section, in which 1 V rms voltage is applied to the electrodes. As shown in the deformed displacement plot, this corresponds to the S0 Lamb-wave mode of the acoustic resonator. Strain and electric field profiles contributing to the n_1 index change are plotted in the location of the integrated optical waveguide. Using the weighting of these fields against the optical mode profile, we determine

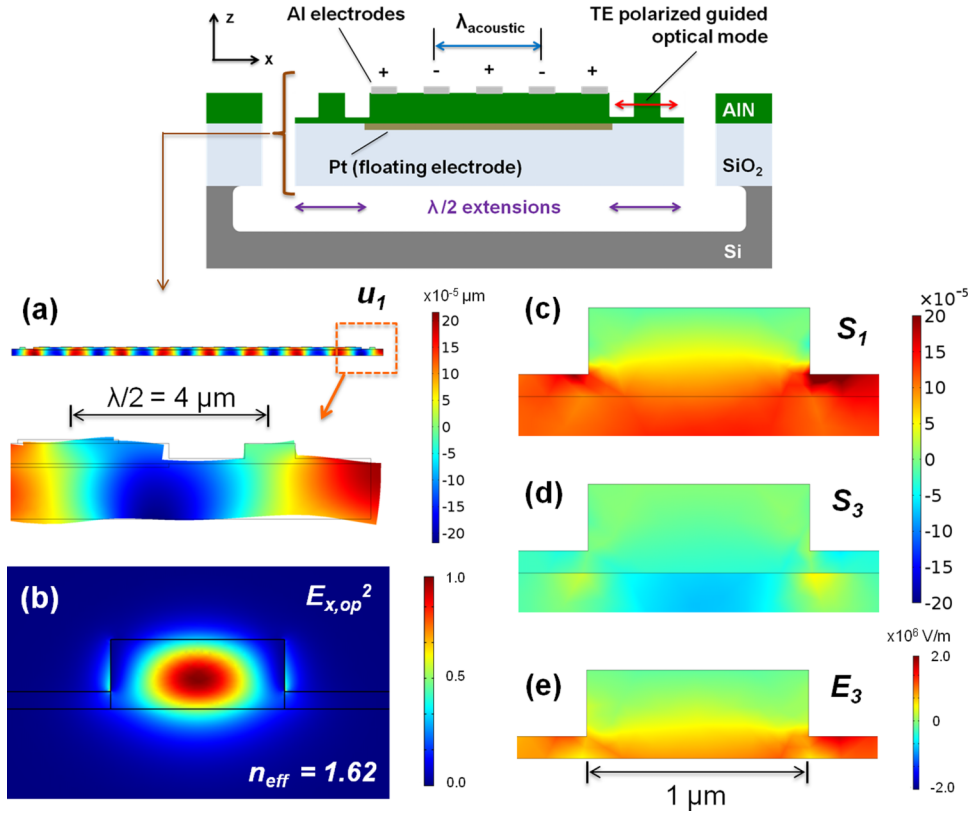

FIG. 2. Schematic representation of the modulator cross-section, where the integrated optical waveguide forming part of a photonic racetrack resonator is centered at a position corresponding to the placement of a virtual CMR electrode. COMSOL FEM simulations of: (a) lateral displacement profile for modulator with zoomed in section showing deformation of S0 mode (scaled 1000×), (b) TE polarized optical mode in integrated waveguide showing spatial profile of $E_{x,op}{}^2$, and distribution in waveguide section of (c) strain S_1 (S_{xx}), (d) strain S_3 (S_{zz}), and (e) electric field E_3 (E_z).

values of 2.54×10^{-5}, -8.11×10^{-6}, and 1.43×10^5 V/m for $S_{1,eff}$, $S_{3,eff}$, and $E_{3,eff}$, respectively (where the maximum strain produced in the device cross-section is 2.23×10^{-4}). While the $p_{13}S_{3,eff}$ and $r_{13}E_{3,eff}$ contributions are opposite in sign to $p_{11}S_{1,eff}$, their contributions to Δn_1 are 1-2 orders of magnitude lower. Thus we can verify the device is primarily modulated through the change in refractive index generated by the p_{11} elasto-optic coefficient. The refractive index of AlN for the telecom L-band wavelengths used in this work is ~2.0, which suggests a total Δn_1 on the order of 9.15×10^{-6}. Hence, the modulation of the in-plane material index is the source of Δn_{eff} for the optical wave propagating in the photonic resonator.

In order to determine the output of the experimental device, we consider the effect of Δn_{eff} in the photonic resonator. The resonance condition in the racetrack can be described by $n_{eff}(2\pi R + 2L_A) = m\lambda_o$, where L_A is the length of each arm, R is the bend radius, and m is the mode number for the resonant wavelength, λ_o. Electromechanical excitation of the device while light is coupled in and out of the racetrack results in an optical output modulation, which may be described as follows:

$$P_{\text{mod}} = \frac{dT}{d\lambda} \cdot \frac{d\lambda}{dn_{eff}} \cdot \Delta n_{eff}. \tag{3}$$

Here $dT/d\lambda$ is determined by the slope of the transmission power, where the pump laser is detuned with respect the resonant wavelength, λ_o. The $d\lambda/dn_{eff}$ term is generated by modulation of the optical resonance condition in the integrated section of the waveguide. Since the refractive index change is generated in a single arm and not uniform throughout the resonator, we estimate the contribution as $\frac{d\lambda}{dn_{eff}} \approx \left[\frac{L_A}{(2\pi R+2L_A)}\right]\frac{\lambda_o}{n_{eff}}$. Based on this approach, we can assess the ability of this device to act as an optical intensity modulator.

Devices are fabricated following a previously developed partial etch process[8] with some modifications. To begin, 1.1 μm silicon dioxide is thermally grown on a 4 in. high-resistivity (20 000 Ω cm) silicon wafer to serve as the under-cladding layer for the guided optical wave. The bottom floating electrode plates are patterned with stepper lithography (Nikon G4) and a lift-off process is applied to define 75 nm platinum (Perkin Elmer 6J sputter deposition). This is followed by RF sputtering (Tegal AMS) of 400 nm AlN. This thickness was previously selected in the development of photonic resonators,[18] and x-ray diffraction rocking curves confirm a high degree of orientation for the thin film with a full-width half-maximum of 1.59° around the AlN 36° peak. The top electrodes and pads are patterned next followed by a lift-off of 75 nm aluminum (CVC Connexion sputter deposition). The major feature definitions for the device are then patterned, including outlines for the acoustic resonator, the photonic racetrack, and the bus waveguides. The outline for these features is partially etched in AlN with Cl_2/BCl_3 chemistry (Plasma-Therm Versaline ICP) down to a slab thickness of 100 nm, which enables all photonic transmissions to occur in rib-type waveguides. A second etch step follows, in which release windows are patterned on either side of the acoustically resonant plate, and the 100 nm AlN slab is removed to expose the underlying oxide. The wafer is then diced to allow processing of individual dies with electron beam lithography to define the small features required on the photonic end of the device. Namely, this involves the definition of grating couplers for the input and output, and a 50 nm gap between the racetrack resonator and the coupling waveguide. These features are then also etched down to the 100 nm slab thickness. At this point no further lithography is required, and oxide under the release windows is removed with an HF-based etch to expose the silicon substrate. Finally, the devices are released with the use of XeF_2 to completely undercut the plates along their width, while they remain fully anchored in the direction of their length.

Optical intensity modulation is experimentally verified with the test setup found in Fig. 1. The acoustic and photonic resonances of the devices are first tested individually for characterization purposes. This information is then used for setting the RF frequency and laser bias wavelength in the electrically driven optical response. Devices with the two different acoustic wavelengths were

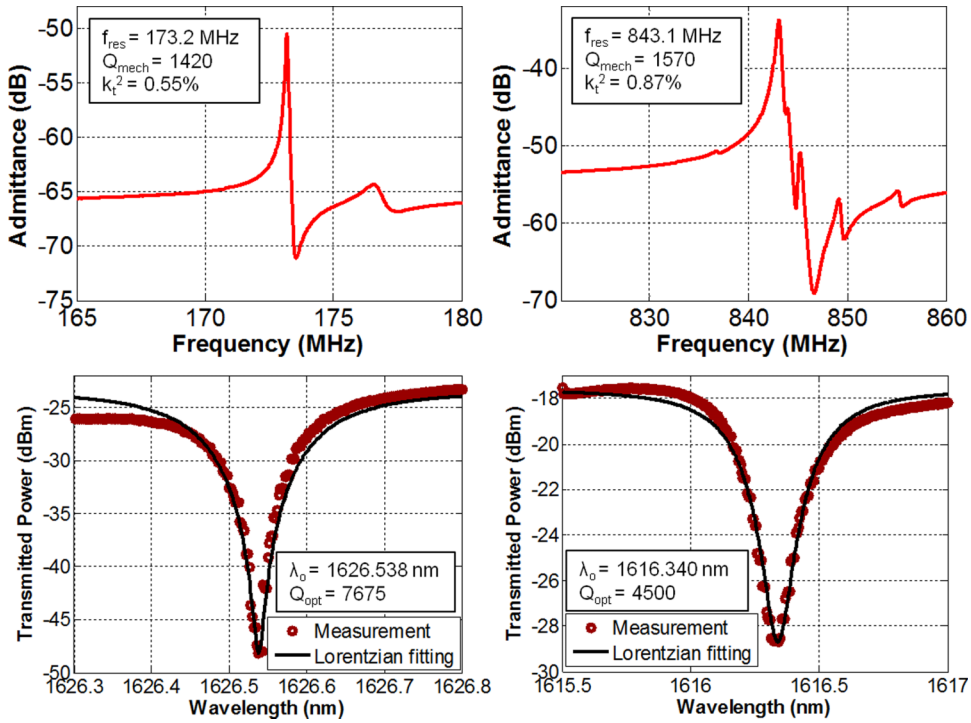

FIG. 3. Acoustic and optical resonance data for devices with acoustic wavelength of 20 μm (left) and 8 μm (right). Electromechanical admittance data show acoustic resonances at 173.2 MHz and 843.1 MHz for the laterally vibrating Lamb mode. Optical resonances in the L-band are selected for the corresponding devices for pump laser cavity detuning.

tested electrically by collecting S_{11} data in a one-port configuration. The device admittances (in dB and normalized to 1 S) extracted from the S_{11} measurements are shown in Fig. 3. The fundamental Lamb wave mode appears at 173 MHz and 843 MHz for the two devices, with mechanical quality factors of 1420 and 1570, respectively. On the photonic end, optical insertion loss measurements are collected with a tunable laser (Santec TSL-510) and power meter (Exfo PM-1103) to identify optical resonances through the racetrack resonator that may be biased for the experiment. TE mode propagation is selected with the use of polarization paddles that feed into the input grating via single mode fiber. The racetrack waveguide width differs for the two devices tested, with a wider 3 μm waveguide used for the 173 MHz device, and 1 μm used in the 843 MHz device (indicated in Fig. 2). As shown in Fig. 3, near critically coupled (extinction ratios >10 dB) optical resonances at 1626.538 nm and 1616.340 nm are selected for the two devices. The transmission data are least square fit to a Lorentzian function, and the tested resonators exhibit loaded optical quality factors of 7670 and 4500, respectively. Here, the transmission data have not been normalized (the power level directly impacts $dT/d\lambda$) and the majority of insertion losses are produced by grating coupler transmittance and fiber alignment.

Elasto-optic modulation is tested by using the vector network analyzer (VNA) to measure the S_{21} insertion loss of the device. Electrical excitation is supplied from the 1st port, while the pump laser is detuned with respect to the optically resonant wavelength. The response from the output grating is fed into an avalanche photodetector (APD—New Focus 1647) with a conversion gain of 6000 V/W and supplied back to the 2nd port of the VNA. S_{21} responses are shown for the two devices in Fig. 4, for an input RF power level of −10 dBm. As anticipated, the peaks correspond to those seen in the electromechanical admittance plots. It may also be noted that several of the spurious mechanical modes appearing in the admittance data also show up in the S_{21} optical response. This suggests strong overlap with the guided optical wave which can be

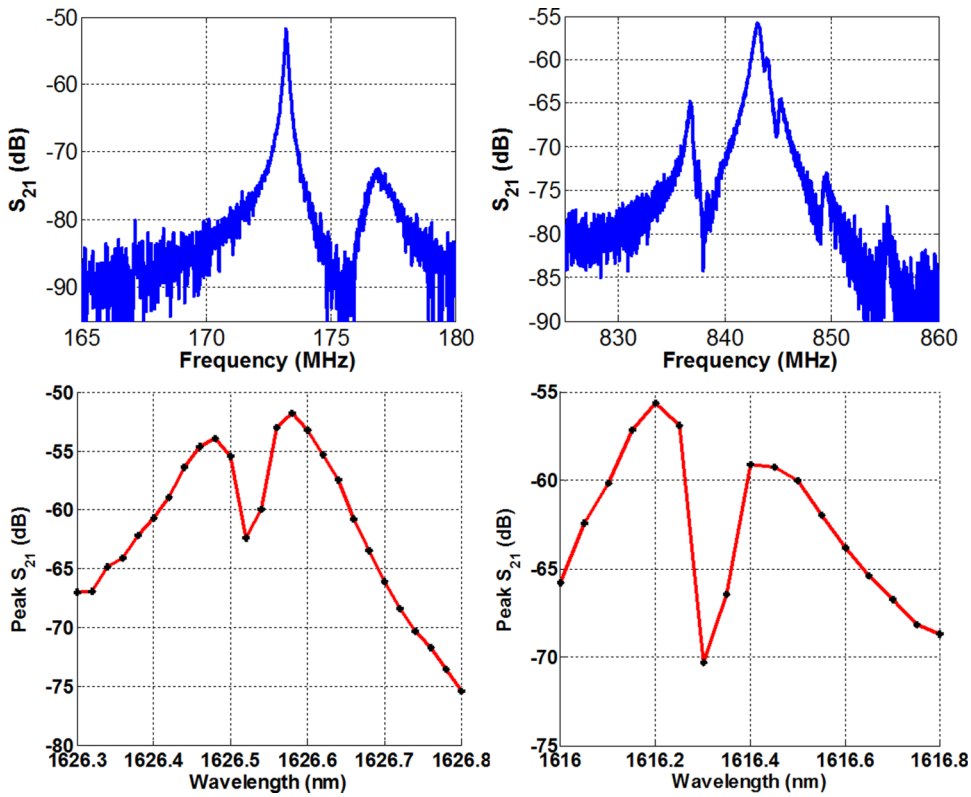

FIG. 4. (Left) S_{21} response measured for elasto-optic modulation with 20 μm acoustic wavelength at cavity detuned optical wavelength of 1626.58 nm. (Right) S_{21} response measured for 8 μm acoustic wavelength at cavity detuned optical wavelength of 1616.225 nm. Corresponding peak S_{21} values measured with respect to optical wavelength is shown below for each device.

identified and mitigated based on the mode of vibration.[22,23] In addition, the peak S_{21} as a function of cavity detuning is also shown for the two devices in Fig. 4. Based on the experimental values ($dT/d\lambda = 3.5 \times 10^4$ W/m and 6.9×10^4 W/m, $d\lambda/dn_{eff} = 2.5 \times 10^{-7}$ and 2.3×10^{-7}, for the 173 MHz and 843 MHz devices, respectively), we can estimate a Δn_{eff} of approximately 5.9×10^{-6} for the device at 173 MHz and 1.1×10^{-6} for the device at 843 MHz. This is on the order of the simulated value for Δn_1, considering the applied voltage. The RF slope efficiency of the intensity modulation (dT/dV) for the two devices is 4.3×10^{-7} W/V and 2.7×10^{-7} W/V at 173 MHz and 843 MHz, respectively. As the output modulation is a function of the optical resonator, improvements in the optical quality factor or waveguide to resonator coupling will directly increase the modulation depth (via $dT/d\lambda$). The corresponding wavelength shift per input voltage for the detuning conditions in Fig. 4 is 12.1 pm/V in the 173 MHz device and 3.9 pm/V in the 843 MHz device.

In conclusion, we have demonstrated elasto-optic modulation in a fully integrated device with the use of a laterally vibrating acoustic resonator. By incorporating a photonic resonator directly into the body of the Lamb wave device, we are able to efficiently utilize the strain energy produced, and overlap this field with the guided optical mode. The design and fabrication process described allows the elasto-optic interaction to be localized in the thin film AlN. At the same time, the acoustic and photonic sections are sufficiently decoupled to prevent conflicts that arise from the co-manufacturing of these device types and the modulation is not limited by physical displacements.[8] By extending the designs of laterally vibrating contour mode resonators, it should also be possible to operate this device at higher frequencies. This enables a new platform to study photon-phonon interactions in the field of optomechanics. In addition, these optical modulators may be monolithically integrated with other components to be implemented in an RF-photonic link.[24] As a result, they may be of interest for a variety of RF and microwave photonics applications.[25]

The authors would like to acknowledge process related support from the staff at the Carnegie Mellon Nanofabrication Facility as well as funding support from the National Science Foundation (Award No. ECCS-1201659) and DARPA under the MESO program (Award No. FA86501217624).

[1] C. S. Tsai, IEEE Trans. Circuits Syst. **26**, 1072 (1979).
[2] A. Korpel, *Acousto-Optics*, 2nd ed. (CRC Press, 1996).
[3] M. Eichenfield, J. Chan, R. M. Camacho, K. J. Vahala, and O. Painter, Nature **462**, 78 (2009).
[4] G. Bahl, J. Zehnpfennig, M. Tomes, and T. Carmon, Nat. Commun. **2**, 403 (2011).
[5] J. Xu and R. Stroud, *Acousto-Optic Devices: Principles, Design, and Applications* (Wiley, 1992).
[6] D. A. Fuhrmann, S. M. Thon, H. Kim, D. Bouwmeester, P. M. Petroff, A. Wixforth, and H. J. Krenner, Nat. Photonics **5**, 605 (2011).
[7] J. Bochmann, A. Vainsencher, D. D. Awschalom, and A. N. Cleland, Nat. Phys. **9**, 712 (2013).
[8] S. Ghosh and G. Piazza, Opt. Express **23**, 15477 (2015).
[9] C. Baker, W. Hease, D.-T. Nguyen, A. Andronico, S. Ducci, G. Leo, and I. Favero, Opt. Express **22**, 14072 (2014).
[10] K. C. Balram, M. Davanço, J. Y. Lim, J. D. Song, and K. Srinivasan, Optica **1**, 414 (2014).
[11] M. M. de Lima and P. V. Santos, Rep. Prog. Phys. **68**, 1639 (2005).
[12] M. M. de Lima, M. Beck, R. Hey, and P. V. Santos, Appl. Phys. Lett. **89**, 121104 (2006).
[13] S. A. Tadesse and M. Li, Nat. Commun. **5**, 5402 (2014).
[14] D. Royer and E. Dieulesaint, *Elastic Waves in Solids I: Free and Guided Propagation* (Springer Science & Business Media, 1999).
[15] G. Piazza, V. Felmetsger, P. Muralt, R. H. Olsson III, and R. Ruby, MRS Bull. **37**, 1051 (2012).
[16] M. Rinaldi, C. Zuniga, C. Zuo, and G. Piazza, IEEE Trans. Ultrason. Ferroelectr. Freq. Control **57**, 38 (2010).
[17] S. Y. Davydov, Semiconductors **36**, 41 (2002).
[18] S. Ghosh and G. Piazza, J. Appl. Phys. **113**, 016101 (2013).
[19] C. Xiong, W. H. P. Pernice, and H. X. Tang, Nano Lett. **12**, 3562 (2012).
[20] J.-B. You, M. Park, J.-W. Park, and G. Kim, Opt. Express **16**, 18340 (2008).
[21] P. Gräupner, J. C. Pommier, A. Cachard, and J. L. Coutaz, J. Appl. Phys. **71**, 4136 (1992).
[22] D. Branch, K. Wojciechowski, and R. Olsson, IEEE Trans. Ultrason. Ferroelectr. Freq. Control **61**, 729 (2014).
[23] S. Gong and G. Piazza, IEEE Trans. Electron Devices **60**, 3888 (2013).
[24] R. C. Williamson and R. D. Esman, J. Light. Technol. **26**, 1145 (2008).
[25] D. Marpaung, C. Roeloffzen, R. Heideman, A. Leinse, S. Sales, and J. Capmany, Laser Photonics Rev. **7**, 506 (2013).